steel research international

steel research international

RESEARCH ARTICLE OPEN ACCESS

Agglomeration Behavior of Nonmetallic Particles on the Surface of Si-Killed Liquid Steel Using HT-CSLM: An In Situ Investigation

Suwam Kumar[1] | Muhammad Nabeel[1] | Angshuman Podder[1] | Andre B. Phillion[1] | Neslihan Dogan[2]

[1]Materials Science Engineering, McMaster University, Hamilton, Canada | [2]Materials Science Engineering, Delft University of Technology, Delft, Netherlands

Correspondence: Suwam Kumar (kumars66@mcmaster.ca)

Received: 21 October 2025 | **Revised:** 8 January 2026 | **Accepted:** 22 January 2026

Keywords: agglomeration | high-temperature confocal scanning laser microscopy | inclusions | Si-killed steel | steel cleanliness

ABSTRACT

While extensive research has focused on the agglomeration of Al_2O_3 inclusions in low-carbon, Al-killed steels, the behavior of non-Al_2O_3 inclusions in Si- and Si/Mn-killed steels remains poorly understood—despite their widespread industrial use and importance for steel cleanliness. This study investigates the in situ agglomeration of semisolid Al–silicate inclusions in Si-killed steel using high-temperature confocal scanning laser microscopy. Particle velocity, acceleration, and attractive forces at the steel/argon interface were measured directly. A modified capillary interaction model, based on the Kralchevsky–Paunov framework, was applied to calculate interparticle forces and showed good agreement with experimental results. Compared to Al_2O_3 inclusions in Al-killed steel, Al–silicate inclusions exhibited significantly weaker attractive forces (10^{-16} to 10^{-15} N) and a shorter interaction range (~34 μm), indicating a lower tendency to agglomerate. These findings highlight key differences in inclusion behavior between steel types and confirm the model's applicability to semisolid systems.

1 | Introduction

The importance of producing "clean" steel has increased drastically to meet customer demand. In steelmaking, "clean steel" refers to steel with minimal impurities and nonmetallic inclusions in terms of size, composition, shape, distribution, and amount [1]. The inclusions that remain in the liquid steel can agglomerate and form clusters. These clusters can obstruct molten steel flow, causing disruptions, reduced productivity, and nozzle blockages [2]. They can also degrade mechanical properties, leading to reduced strength, ductility, and toughness as they can act as stress concentration sites within the steel matrix, and may serve as initiation points for cracks and fractures, potentially leading to steel component failure [3]. Effective steelmaking practices and quality control measures are crucial to mitigate issues related to inclusion clusters. This involves optimizing refining processes, implementing inclusion control techniques (e.g., calcium treatment), and ensuring proper maintenance of nozzles and flow passages to produce clean steel [4, 5].

Si and Si/Mn-killed steel are widely utilized in various industries for their favorable properties, such as enhanced cleanliness, reduced inclusion content, and superior mechanical properties, including strength, toughness, and ductility [6]. Silicon acts as an efficient deoxidizer, while manganese improves hardenability and overall strength. These characteristics make them well-suited for demanding applications in automotive, structural, and manufacturing sectors, particularly in the construction of buildings, bridges, and long products such as channels, angles, pipes, mechanical tubes, and electrical conduits [7, 8]. During the production of these steel products, Si/Mn are used as deoxidizers that remove oxygen from molten steel, forming oxide inclusions such as SiO_2, $MnO–SiO_2$, and $MnO–SiO_2–Al_2O_3$ [9]. In Si/Mn-killed steels, these inclusions are generally liquid at steelmaking temperatures and exhibit lens-like morphologies,

which reduces their tendency to agglomerate. However, due to the complex reactions involved in steelmaking, interactions with residual aluminum from alloying additions or refractory materials can lead to the formation of complex aluminosilicate phases such as mullite ($3Al_2O_3{\cdot}2SiO_2$) or anorthite ($CaO–Al_2O_3{\cdot}2SiO_2$), which may cluster near the slag–metal interface and cause nozzle clogging or surface quality deterioration [9]. In addition, different types of solid or complex inclusions may also originate from ladle glaze, refractory erosion, slag entrainment, or minor alloying additions such as Al, Mg, and Ca [10].

Prior studies [11–15] using high-temperature confocal scanning laser microscopy (HT-CSLM) have investigated the agglomeration behavior of a wide range of inclusion chemistries, including Al_2O_3, $Al_2O_3–SiO_2$, $CaO–Al_2O_3$, $Al_2O_3–MnO$, $CaO–SiO_2–Al_2O_3$, and $Al_2O_3–MnO–SiO_2$, as well as sulfide-based inclusions such as CaS–MnS. Among these, Yin et al. [11] compared solid Al_2O_3 inclusions with alumina-rich (80% $Al_2O_3–SiO_2$) solid particles and observed that the presence of silica weakens the interparticle attractive forces by modifying their interaction characteristics, thereby reducing both the strength and effective range of attraction. Pure alumina inclusions were found to interact over distances up to 50 μm, while alumina-rich SiO_2 containing inclusions demonstrated a notably shorter interaction range. In a follow-up study [12], they investigated the agglomeration of $CaO–Al_2O_3–SiO_2$ (CAS) inclusions and found that solid inclusions, such as CA80S and CAS95 (the numerals after each abbreviation denote the average mass fraction of the respective components within the inclusion particles), exhibited strong capillary attraction leading to agglomeration, with interaction ranges extending up to 100 μm. In contrast, liquid inclusions like CA60S showed negligible attraction, which the authors attributed to their lens-like morphology and the resulting inhibition of capillary-driven interactions. These studies, however, were conducted on industrial samples and under relatively low oxygen conditions, limiting their applicability to high oxygen environments or semisolid inclusion states.

Further insights were provided by Tanaka et al. [13], who investigated the agglomeration behavior of CaS, MnS, and $CaO–Al_2O_3–SiO_2$ inclusions in Si-killed, Ca-treated high-carbon steel. They reported that sulfide inclusions (MnS and CaS) exhibited weak attractive forces ranging from 10^{-16} to 10^{-17} N. Semiliquid oxide inclusions ($CaO–Al_2O_3–SiO_2$) did not agglomerate under these conditions, as they were rapidly encapsulated by surrounding sulfides, preventing effective capillary interaction. Similarly, Vantil et al. [15] identified two distinct interaction modes at the steel-gas interface. Solid, irregular $MnO–Al_2O_3$ inclusions exhibited strong capillary-driven agglomeration, with interaction distances up to 40–50 μm and force magnitudes consistent with the Kralchevsky–Paunov capillary interaction model. In contrast, spherical liquid inclusions ($Al_2O_3–MnO–SiO_2$) showed negligible interaction, reinforcing the importance of solid morphology and interfacial properties in capillary attraction. More recently, Mu et al. [16] proposed a refinement to the Kralchevsky–Paunov model to better account for particle shape and contact angle effects, improving predictive capability for nonmetallic inclusions at the steel/gas interface. However, this revised model has not yet been validated for semisolid inclusions nor applied to Al–silicate systems.

While previous studies have investigated the agglomeration behavior of inclusions in Si- and Si/Mn-killed steels, the in situ observation of Al–silicate agglomeration, particularly in semisolid form and under high-oxygen conditions, remains unexplored. This is a significant gap, given the role of Al–silicates in long product manufacturing and their tendency to form agglomerates that contribute to nozzle clogging. A more detailed understanding of their agglomeration behavior is essential to improve Si/Mn-killed steel cleanliness and minimize operational disruptions.

To address this, the present study employs high-temperature confocal scanning laser microscopy (HT-CSLM) to observe the motion, interaction, and agglomeration dynamics of semisolid Al–silicate inclusions at the liquid steel/argon interface. Direct in situ observation enables measurement of particle trajectories, interparticle distances, and interaction times, providing critical insight into dynamic agglomeration mechanisms. These measurements are evaluated using the refined capillary interaction model developed by Mu et al. [16], which incorporates the effects of particle shape and contact angle to improve predictive accuracy for inclusion behavior at the steel/gas interface.

In addition to characterizing attractive force magnitudes and acting distances, the study also explores how oxygen-induced supersaturation and holding time influence inclusion morphology. Finally, the agglomeration behavior of Al–silicate inclusions in Si-killed steel is compared with that of Al_2O_3 inclusions in Al-killed steel. This comparative analysis reveals key differences in interfacial interactions and agglomeration tendencies, providing insight into clogging risk and guiding future strategies for inclusion control in different steel chemistries.

2 | Experimental Methodology

2.1 | Melt Preparation, Composition, and Inclusion Analysis

A set of synthetic steel samples for in situ HT-CSLM experiments was prepared using a resistance-heated vertical tube furnace, following the methodology detailed by Podder et al. [17]. A 297 g Fe-O melt was processed under controlled atmospheric conditions and deoxidized with Fe80Si(1.2 wt%Al), with time-sequenced sampling at 30, 60, 300, and 600 s followed by rapid quenching. All deoxidation experiments were conducted at a temperature of 1600°C under a high-purity argon atmosphere (99.999%). The argon gas was purified by passing through titanium turnings at 700°C (0.5 L min^{-1}), maintaining the furnace oxygen partial pressure below $\sim 10^{-12}$ atm. The 300-s sample, selected for its relatively low inclusion number density and total oxygen content (250 ppm), was further characterized and used for in situ observation. (Samples from 30, 60, and 600 s were used in other studies.) Bulk composition was measured using induction coupled plasma optical emission spectroscopy (Pro CCD simultaneous ICP-OES); carbon (C) and sulfur (S) levels were determined by combustion analysis (LECO CS744); and the total oxygen (T.O.) and nitrogen (N) contents were measured using the inert gas fusion method (LECO ON736 model). The measured composition is given in Table 1. Subsequently, a disc 5 mm dia. × 300 μm in thickness was prepared (ground, polished, and ultrasonically cleaned) for the in situ CSLM experiment.

2.2 | In Situ Experiment

High-temperature confocal scanning laser microscopy (HT-CSLM, Lasertec VL2000DX) was used to observe inclusion agglomeration

TABLE 1 | Measured compositions (wt%) for (a) Al–silicate inclusions (average value) and (b) steel sample used in the in-situ CSLM experiment.

Composition	C	Si	Mn	S	Al	O	Fe
Inclusion	—	27.7	—	—	19.4	49.7	1.8
Steel	0.008	0.14	0.045	0.0015	0.004	0.025	bal

in situ, following procedures outlined in prior studies [18–22]. The system uses a He-Ne laser for imaging and an infrared image furnace for heating. Steel samples were placed inside high-purity alumina crucibles (5.0-mm inner diameter), which were positioned on a gold-plated ellipsoidal sample holder. The HT-CSLM apparatus consists of a vertically aligned microscope for real-time imaging, an IR furnace below the stage for precise temperature control, and a gas purification unit that supplies high-purity argon to the furnace chamber, preventing oxidation during observation.

Observing inclusions at the liquid surface of a steel sample presents challenges due to the difficulty of forming a flat liquid pool. When molten, surface tension causes the steel to adopt a hemispherical shape, complicating inclusion observation. To overcome this, an inverse "V"-shaped temperature profile, as described by Griesser et al. [23], was employed to create a nearly flat liquid surface (Figure 1). This profile is achievable only by using very thin disc-shaped samples (0.3–0.4 mm thick), which promote a strong radial temperature gradient while maintaining a weak gradient through the thickness. This configuration keeps the center of the disc above the melting point while the edges remain solid, resulting in a stable liquid pool surrounded by a solid rim and enabling reliable in situ observation of inclusions at the steel/argon interface. A schematic of side view of the sample and the furnace chamber showing the temperature profile is given in Figure 1. Due to the high thermal conductivity of liquid steel, the small dimensions of the molten pool, and the presence of natural convection, the temperature within the central observation region is expected to remain relatively uniform during the experiment. Although a radial temperature gradient exists as a result of the CSLM furnace configuration, it is primarily localized near the solid–liquid interface. At the local scale relevant to inclusion–inclusion interactions at the steel/Ar interface, temperature and surface-tension variations are therefore sufficiently small, minimizing thermocapillary effects, such that capillary attraction remains the dominant agglomeration mechanism.

Before heating, the chamber underwent a series of preparatory steps to establish a low-oxygen atmosphere. It was first purged with 5N purity argon gas (99.999%) at a flow rate of 50–60 mL/min, followed by evacuation to remove residual air. This purge-and-vacuum cycle was repeated three times to ensure effective cleaning. The argon gas was further purified using a gas cleaning system to eliminate moisture and trace impurities. To minimize reoxidation during heating, a 0.010-mm thick titanium (Ti) foil was wrapped around the upper exterior of the alumina crucible. Based on prior work by Mu et al. [16] using the same setup, the resulting oxygen partial pressure during experiments was estimated to range between 3 and 30 $\times$ 10^{-20} kPa over the temperature range of 1400°C to 1600°C.

The heating profile involved a stepwise increase in temperature from room temperature to 1500°C using five different heating rates, followed by a final manual adjustment, as shown in Figure 2. This manual adjustment was used to gradually raise the temperature above 1500°C until a small liquid pool with visible inclusions appeared in the CSLM image. Inclusion tracking began once the inclusions became mobile within the liquid pool. Agglomeration behavior was observed over the next ≈45 s, by recording a sequence of images of the metal surface at 15 Hz, using a 10× objective, capturing 1024×1024 pixel images with a pixel size of 0.47 μm. This defines the minimum resolvable displacement and ensure precise position measurements relative to inclusion sizes and spacing. The sample was then rapidly quenched to preserve the resulting agglomerated structures.

Prior to the agglomeration experiment, a separate trial using the same steel sample was conducted under identical thermal conditions to verify the chemical composition of the inclusions and confirm the presence of Al–silicates. The sample was heated following the procedure described above until inclusions appeared in the liquid pool, at which point it was rapidly quenched. The quenched specimen was examined using a JEOL 6610LV scanning electron microscope equipped with energy-dispersive X-ray spectroscopy (SEM-EDS). Elemental analysis confirmed the inclusions to be Al–silicate based on the consistent detection of aluminum, silicon, and oxygen. A total of 40 inclusions were analyzed using both EDS

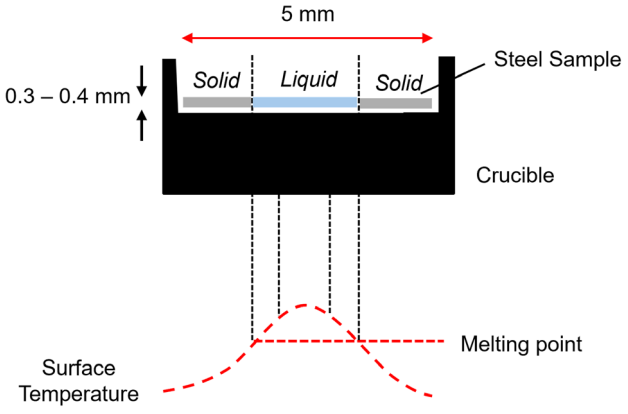

FIGURE 1 | Schematic illustration of sample dimension and temperature profile on the sample surface in CSLM (side view).

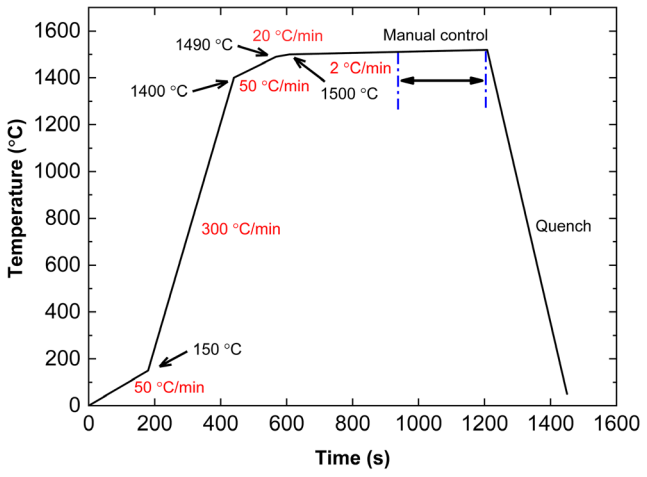

FIGURE 2 | Temperature profile of in situ observation of inclusion agglomeration.

mapping and point analyses, revealing uniform composition across all inclusions. The average composition is reported in Table 1.

2.3 | Data Analysis

Analysis of the HT-CSLM image data was performed using the ImageJ software package [24]. Each frame was binarized and processed to extract the center of mass, projected area, and perimeter of each visible inclusion. These measurements were used to quantify the inclusion size, center-to-center distance, and circularity of the inclusions.

Circularity, CF_k, was calculated using the following expression:

$$CF_k = \frac{4\pi A_k}{P_k^2} \quad (k = 1, 2) \tag{1}$$

CF_k is a dimensionless shape factor used to characterize inclusion morphology, where a value of 1 corresponds to a perfect circle. In this expression, A_k and P_k represent the projected area and perimeter of inclusion k, respectively.

In addition to morphological analysis, dynamic motion data extracted from HT-CSLM videos were used to evaluate the attractive forces between inclusions during agglomeration. An illustrative force calculation is presented in Figure 3. This method applies Newton's second law of motion, using measured particle accelerations and estimated masses to compute interparticle forces, as detailed in Equations (2)–(5). A more comprehensive explanation of this approach can be found in the work of Nakajima and Mizoguchi [25].

$$a_i = (V_{i+1} - V_i)/\Delta t_i = (d_{i+1}/t_{i+1} - d_i/t_i)\Delta t_i \tag{2}$$

$$\Delta t_i = (t_{i+1} - t_i) \tag{3}$$

$$m_2 = (4/3) \times \pi \times R_2 \times R_2 \times R_2 \times \rho \tag{4}$$

$$F_{A,i} = m_2 \times a_i \times m_1/(m_1 + m_2) \tag{5}$$

$$R_k = \sqrt{A_k/\pi} \tag{6}$$

In this framework, m_1 and m_2 denote the masses of the host and guest inclusions, respectively, while a_i represents the acceleration at each time point t_i. The velocity of the inclusion at time t_i is given by V_i, and d_i is the center-to-center distance between inclusions. To characterize irregularly shaped inclusions, the equivalent radius R_2 was used, defined as the radius of a circle with the same projected area (Equation (6)). If only the guest inclusion moves, the force is calculated using its mass and acceleration. When both inclusions move toward one another, the net force is determined using the combined acceleration and mass terms, as described in Equation (5).

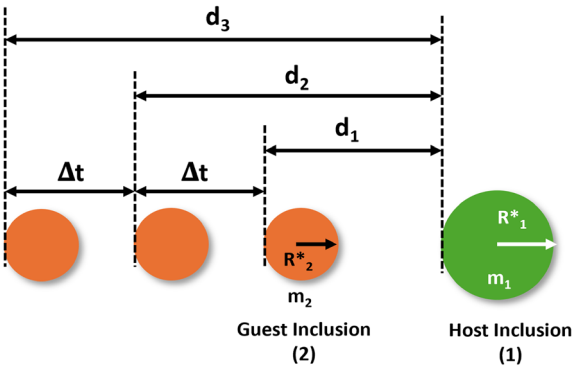

FIGURE 3 | Schematic illustration to calculate the attractive force from the observed change in position of inclusions pair in CSLM Video, adapted from Refs. [11, 12, 25, 26].

2.4 | Capillary Force Model

Capillary interaction is widely recognized as the primary driver of inclusion clustering in molten steel [25–28]. These interactions arise from meniscus deformation at the gas–liquid interface, generating attractive forces between inclusions—a phenomenon well established in colloidal systems. To quantify these forces, the present study adopts a theoretical model based on the framework developed by Kralchevsky et al. [29], who derived energy and force balances for particles floating on liquid surfaces. Paunov et al. [18] subsequently simplified this approach to estimate capillary interaction energy and force between spherical particles at gas–liquid interfaces. Figure 4 illustrates the force components acting on two spherical inclusions of radii R_1 and R_2, positioned at the steel-argon interface [25–28].

The capillary interaction energy between two spherical inclusions ΔW, illustrated in Figure 4, consists of three primary contributions: wetting energy (ΔW_w), meniscus surface tension energy (ΔW_m), and gravitational energy (ΔW_g) [29]. Kralchevsky et al. [29] combined these contributions into the following expression for interaction energy:

$$\begin{aligned}\Delta W = -\pi\gamma\big[&(Q_1 h_1 - Q_{1\infty} h_{1\infty})(1 + O(q^2 R_1^2)) \\ &+ (Q_2 h_2 - Q_{2\infty} h_{2\infty})(1 + O(q^2 R_2^2))\big]\end{aligned} \tag{7}$$

In Equation (7), γ is the surface tension of liquid steel (assumed as 1.2 N/m [30]), Q_k denotes the capillary charge between inclusion k and the molten steel, and $Q_{k\infty}$ represents the theoretical capillary charge assuming the inclusion and molten steel behave as parallel plates. The terms h_k and $h_{k\infty}$ correspond to the meniscus deformations associated with these capillary charges. Additionally, $O(x)$ denotes a zeroth-order approximation function, and q is the capillary length, defined by:

$$q = \sqrt{\frac{(\rho_{steel} - \rho_{gas})g}{\gamma}} \approx \sqrt{\frac{\rho_{steel}\, g}{\gamma}}, \quad \rho_{steel} \gg \rho_{gas} \tag{8}$$

where ρ_{steel} and ρ_{gas} denote the densities of liquid steel and gas, respectively, and g is the acceleration due to gravity.

The parameters Q_k, $Q_{k\infty}$, h_k, and $h_{k\infty}$ are complex mathematical functions fully detailed by Kralchevsky et al. [29], and their application to liquid steel systems is discussed extensively by Nakajima and Mizoguchi [25] and Kimura et al. [26]. Although these expressions are not explicitly presented here, they require values for the contact angles (α_1, α_2) between the respective inclusions and the liquid steel. In this study, a contact angle of 136° [11] was assumed for both α_1 and α_2, consistent with the Al–silicate inclusions studied.

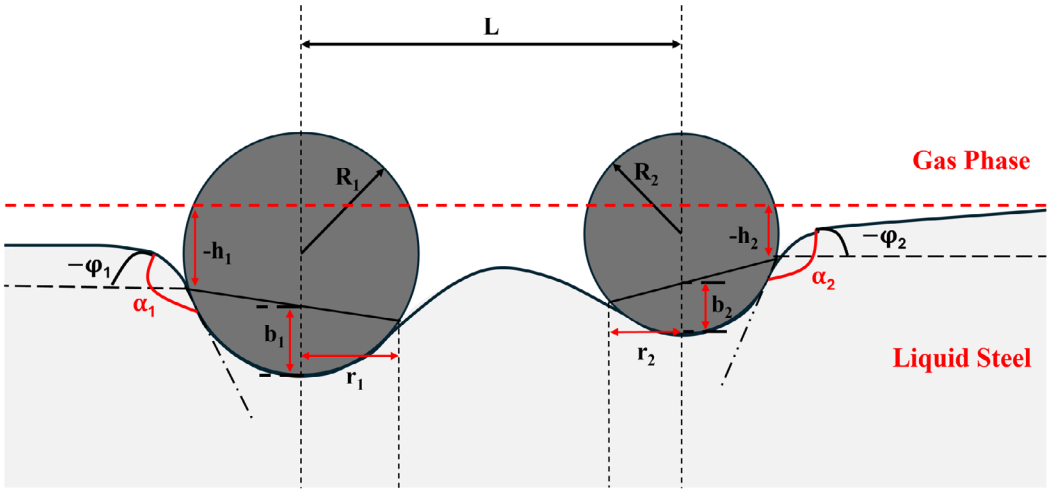

FIGURE 4 | Schematic illustration of the capillary meniscus around two spherical inclusions, adapted from Refs. [25–28].

The capillary force between two inclusions is determined by taking the derivative of the capillary interaction energy ΔW with respect to their separation distance L, as expressed in Equation (9):

$$F = \frac{d(\Delta W)}{dL} \tag{9}$$

Paunov et al. [18] simplified the general formulation (Equations (7)– (8)) and derived the following expression for capillary force, which is valid when the center-to-center distance L lies between the contact line radius r_k (see Figure 4) and the inverse capillary length q^{-1}:

$$F = \frac{2\pi\gamma Q_1 Q_2}{L} \quad (r_k \ll L \ll q^{-1}; k = 1, 2) \tag{10}$$

To improve the accuracy of this approximation, Mu et al. [16] applied L'Hôpital's rule [31], leading to a refined formulation that includes higher-order corrections:

$$F = \frac{2\pi\gamma Q_1 Q_2 (1 - q^2 L^2)}{L} \quad (r_k \ll L; k = 1, 2) \tag{11}$$

Here, the modified model retains the first-order correction from the Bessel function expansion, which Paunov neglected. Using L'Hôpital's rule for small qL, $K_1(qL)$ is approximated as $1/qL - qL$, introducing the $(-q^2L^2)$ term. This correction extends the model's validity range and improves overall accuracy while maintaining key assumptions: rigid, spherical inclusions; constant contact angles; axisymmetric menisci; and negligible hydrodynamic effects. The model exhibits a mathematical singularity as $L \to r_k$, representing the breakdown of the linearized meniscus approximation; however, all experimental measurements were conducted at separations $L > 11.5$ μm, well within the model's validity range where $L \gg r_k$. This revised formulation has been validated for various inclusion types [16, 32, 33].

In the present work, Equation (11) is employed to compare experimentally measured capillary forces between Al–silicate inclusions with theoretical predictions. While the model neglects viscosity of liquid steel in resisting inclusion motion, its influence is minimal under the current conditions because inclusions float at the steel/Ar interface and are not deeply immersed. Other potential resistances, including hydrodynamic drag, Marangoni (thermocapillary) effects, and drainage resistance, are similarly negligible.

3 | Results

3.1 | Observation: Al–Silicate Inclusion Agglomeration and Their Morphological Changes

Quantifying attractive forces between inclusions during agglomeration at the steel/argon interface presents significant experimental challenges. The mirror-polished steel sample was heated under controlled conditions, but inclusion tracking could only begin once surface motion subsided. Early in the experiment, the liquid steel surface exhibited transient flow driven by argon gas convection within the furnace chamber. Inclusion motion could only be resolved once the surface reached a quasi-static state, free from convective disturbances. The CSLM image sequence was initiated at this point (defined as $t = 0$), enabling in situ tracking of inclusion trajectories. From the recorded images, distance, velocity, and acceleration were extracted to calculate the attractive capillary forces acting between inclusions.

Figure 5 shows the agglomeration of two inclusions, accompanied by subsequent morphological changes. The entire sequence from initial inclusion motion to the onset of morphological transformation occurred over approximately 40 s after which the system was quenched directly from 1520°C to room temperature. At this temperature, FactSage 8.0 calculations using the FToxid database predict that the inclusions were in a semisolid/liquid state, with a liquid fraction of approximately 45%.

The agglomeration process is captured in images (a) through (d), where the motion of Inclusion 2 toward Inclusion 1 is clearly evident. The larger inclusion (Inclusion 1) had an equivalent radius of 17 μm, while the smaller inclusion (Inclusion 2) had a radius of 13 μm. Due to their well-defined trajectories and sufficient size, these inclusions were selected for force analysis. In contrast, although numerous smaller inclusions can be seen clustering around the larger ones (suggesting early-stage accumulation and potential coalescence), their extremely small size precluded quantitative tracking or force calculation.

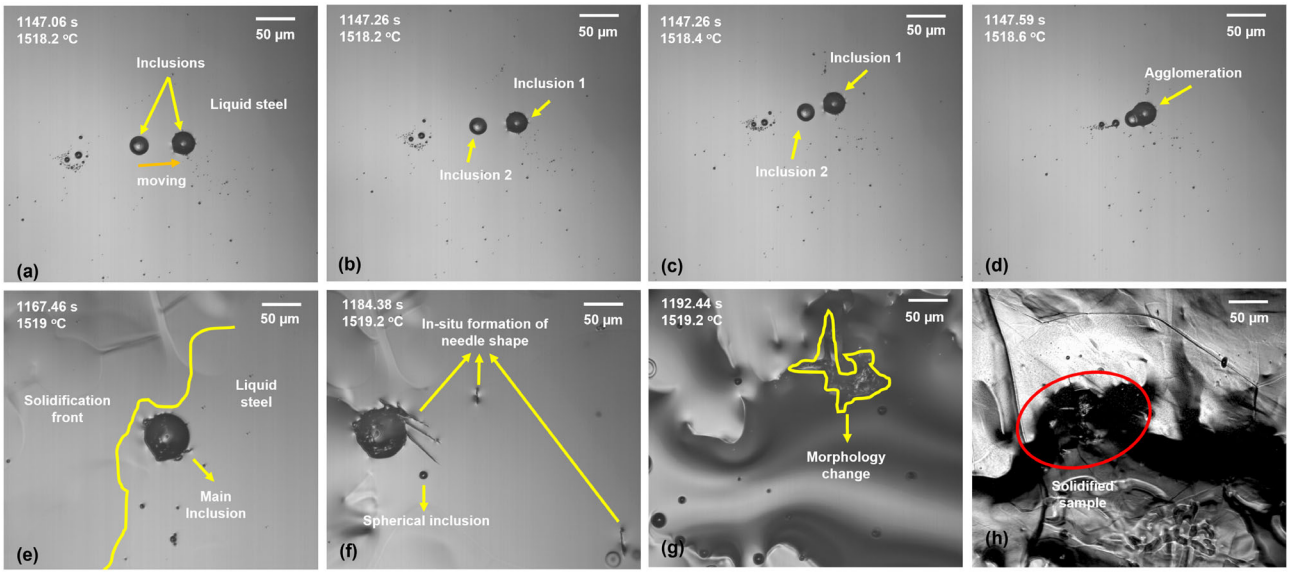

FIGURE 5 | CSLM images showing the agglomeration of two inclusions and their subsequent morphological evolution at the steel/argon interface. (a–d) show the agglomeration process; (e,f) show the changes in inclusion morphology and size; (g,h) show further details of morphological change and solidified sample area. The steel solidification front is also visible in (e).

Following agglomeration, the inclusions underwent noticeable changes in shape and size, as shown in images (e) through (h). The agglomerated inclusion becomes larger (e), develops needle-like features (f), and exhibits increasing irregularity in shape (g). In image (e), an advancing solidification front is also visible. The appearance of needle-like structures in (f) suggests that local thermodynamic conditions such as high supersaturation or elevated oxygen activity may promote anisotropic growth. Finally, image (h) shows the state of the agglomerate after quenching. As seen, the inclusion preserved its morphology and remained in place during the quenching process. A detailed discussion on the development of needle-like morphologies is provided in Section 4.2.

Postquenching, the agglomerated inclusion was analyzed using SEM-EDS to determine their chemical composition. Figure 6 shows the SEM image in (a) and EDS elemental maps (Fe, O, Al, Si) in (c)–(f) of the final inclusion that is shown in Figure 5h. The analysis confirmed that the agglomerated inclusions are mainly Al–silicate, with an average composition of 40% Al_2O_3 and 60% SiO_2. Point analysis was carried out at three locations (A, B, and C) as shown in image (b), with the compositions reported in Table 2.

3.2 | Quantifying the Dynamics of Inclusion Interactions

To evaluate the capillary attraction forces acting between inclusions, the motion of the two primary inclusions shown in Figure 5a–d was tracked frame-by-frame. The inclusion distance were extracted from binarized CSLM images using ImageJ, allowing for the calculation of its distance, velocity, and acceleration as functions of time. Only the two primary inclusions,

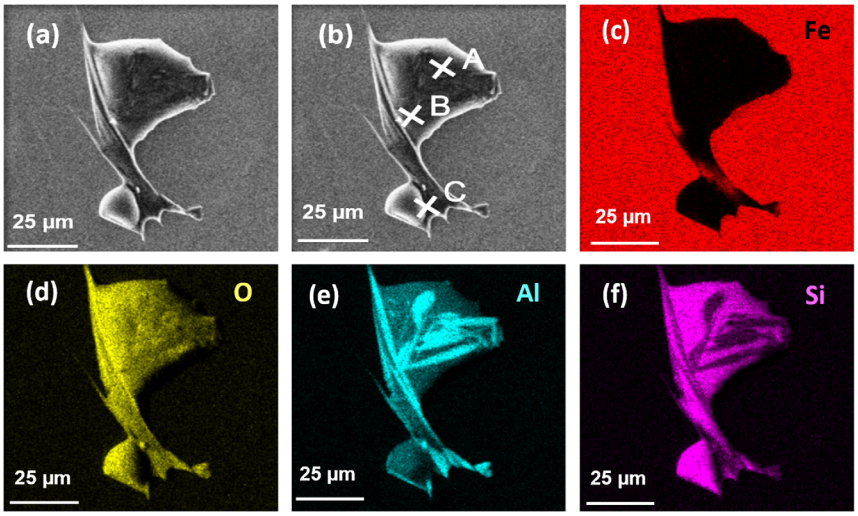

FIGURE 6 | SEM-EDS elemental mapping of agglomerated inclusions after in situ observation experiments: (a) morphology of the agglomerated inclusion; (b) locations of point EDS analysis; and (c–f) elemental mapping of Fe, O, Al, and Si, respectively.

TABLE 2 | EDS point analysis of the agglomerated inclusion.

Location	O (wt%)	Al (wt%)	Si (wt%)
A	49.7	21.9	24.1
B	51.7	16.4	28.7
C	47.6	15.6	32.4

Inclusion 1 (host) and Inclusion 2 (guest), were used for this analysis, as the motion of the surrounding smaller inclusions could not be resolved with sufficient accuracy.

Figure 7 shows the evolution of inter-inclusion distance over time. A marked reduction in separation begins when the distance falls below approximately 35 μm, indicating the presence of a long-range attractive force between the inclusions. To further confirm that this motion was driven by particle interaction rather than steel flow, velocity and acceleration were extracted from the time-series position data and plotted against inter-inclusion distance in Figure 8 on a semilog scale. Analysis revealed that both the velocity and acceleration of the smaller inclusion (i.e., inclusion 2) moving toward the larger one inclusion (inclusion 1) increased as the distance between them decreased, supporting the interpretation that agglomeration was driven by interparticle attraction. If the inclusions were simply following steel flow, the velocity would remain constant as the net acceleration would be negligible.

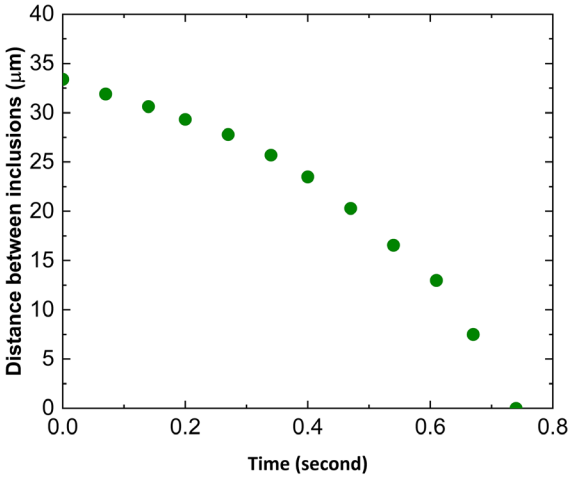

FIGURE 7 | Time evolution of the distance between Inclusion 1 and Inclusion 2, extracted from CSLM video frames.

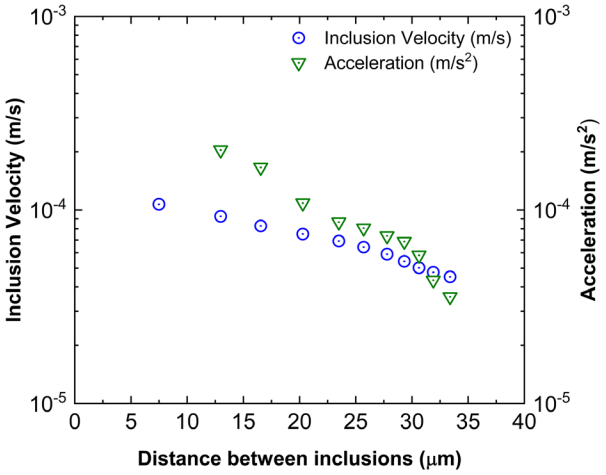

FIGURE 8 | Velocity and acceleration of Inclusion 2 as functions of separation distance from Inclusion 1. Data plotted on a semilogarithmic scale.

4 | Discussion

Below, the measured attractive forces between Al–silicate inclusions are examined, and the observed morphological evolution during agglomeration is interpreted. These results are compared with prior studies and evaluated using a capillary force-based model introduced earlier.

4.1 | Attractive Force Between Al–Silicate Inclusions

The attractive force between inclusions was calculated using Equations (2) – (5), and the resulting force–distance relationship is shown in Figure 9. Experimental results from this study are compared with the data reported by Yin et al. [11] for 80% Al_2O_3–20%SiO_2 inclusions. In the figure, triangles represent the present data points, while the dashed square denotes the range of Yin et al.'s measurements, based on approximately 50 individual observations. The attractive forces observed in this study ranged from 9×10^{-16} to 5×10^{-15} N, increasing with decreasing separation distance. These values are in close agreement with Yin et al., likely due to the comparable particle sizes used in both studies (13–17 μm in the present work versus 2.5–20 μm in Yin's).

Despite the similarity in force magnitude, important differences exist in particle characteristics. Yin et al. examined solid, irregular inclusions with relatively smooth surfaces, whereas the present study focused on globular, semisolid inclusions. The semisolid phase state and rounded morphology may alter the effective capillary charge and wetting behavior at the steel/argon interface, thereby influencing the dynamics of particle interaction. The semisolid inclusions in the current study consist of coexisting solid and

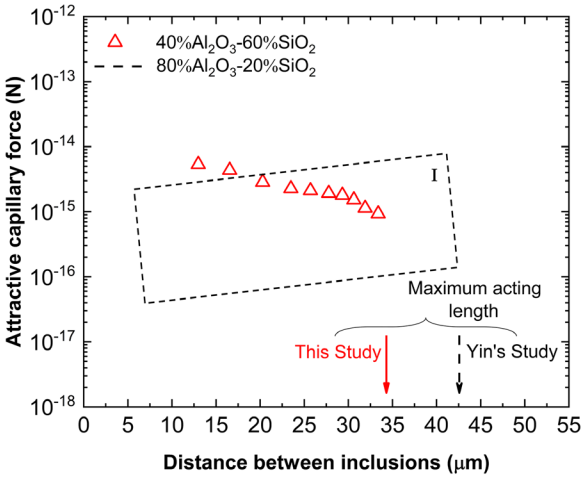

FIGURE 9 | Attractive capillary force as a function of separation distance between Al–silicate inclusion pairs (triangles: present work) and 80% Al_2O_3–20%SiO_2 inclusions reported by Yin et al. [11] (dashed square, I). The calculated maximum acting length for particle–particle interactions is also indicated.

liquid phases without a distinct core–shell structure. Their semisolid nature allows partial deformation of the meniscus, leading to intermediate capillary behavior at the steel/argon interface. Unlike rigid solid inclusions that generate strong capillary attraction, or fully liquid inclusions with negligible meniscus deformation [12], semisolid inclusions exhibit partial meniscus relaxation, reducing the effective capillary charge Q and resulting in intermediate attractive forces.

Also shown in the figure is the calculation of the Maximum Acting Length of the particle–particle interaction, following the methodology of Yin et al. [11]. As can be seen, for the Al–silicate inclusions studied in this work, the maximum acting length was approximately 34 μm, or about 80% of that reported by Yin et al., for the 80%Al_2O_3–20%SiO_2 inclusions. This reduction can be attributed to semisolid nature of inclusion studied in the present work, which lowers interfacial tension and modifies wetting behavior, thereby shortening the effective range of attractive forces. Such composition-dependent variations in interfacial properties are known to strongly influence capillary-driven interactions [12, 25].

Taken together, these results demonstrate that while semisolid Al–silicate inclusions exhibit force magnitudes comparable to solid 80%Al_2O_3–20%SiO_2 particles, their shorter interaction range indicates a reduced tendency to form large agglomerates. This difference highlights the importance of inclusion phase state and interfacial chemistry in controlling agglomeration dynamics in Si-killed steels [12, 25].

4.2 | Large and Irregular Needle-Shaped Inclusion Structure

Beyond the capillary-driven agglomeration mechanisms described previously, another distinct morphological feature observed in this study is the formation of large and irregular needle-shaped inclusions. These structures, exemplified in Figure 6e, can be linked to alumina-rich phases that precipitate under oxygen-rich conditions. The high bulk oxygen content of the present steel (250 ppm) and the extended holding time at elevated temperature may provide a favorable environment for the preferential growth of alumina into elongated, unstable morphologies. Similar observations were reported by Braun et al. [34], who showed that alumina inclusions develop dendritic and needle-like structures under comparable oxygen conditions.

SEM-EDS analysis confirms that these elongated structures contain little to no silica (Figure 6f), suggesting they formed primarily through alumina precipitation in an oxygen-rich melt rather than from pre-existing Al–silicate inclusions. This points to the combined influence of thermodynamic driving forces and kinetic instabilities in shaping inclusion morphology.

The thermodynamic driving force for inclusion growth and transformation in an oxidizing environment can be expressed in terms of oxygen supersaturation (S_a), relative to the equilibrium deoxidation reactions and defined on an activity basis as

$$S_a = \frac{a_O}{a_O^{\mathrm{eq}}} \tag{12}$$

where $a_O = f_O[\%O]$ is the actual oxygen activity in the molten steel and a_O^{eq} is the equilibrium oxygen activity corresponding to a given deoxidation reaction.

For the present steel composition (Table 1) and a dissolved oxygen content of 0.010 wt% (100 ppm) at 1873 K, the calculated supersaturation ratios are Al ($S_a = 6.78$), Si ($S_a = 0.76$), and Mn ($S_a = 7.8 \times 10^{-3}$), based on activity values of $a_{\mathrm{Al}} = 0.0040$, $a_{\mathrm{Si}} = 0.144$, and $a_{\mathrm{Mn}} = 0.045$ in the corresponding equilibrium expressions [35–37]. These results indicate a strong thermodynamic tendency for Al_2O_3 formation, while SiO_2 and MnO are not favored under the prevailing oxygen level (100 ppm), since their supersaturation ratios are below unity ($S_a < 1$). Consequently, alumina is the most stable and preferentially nucleated oxide phase under these conditions.

Furthermore, the high supersaturation condition also governs the inclusion growth morphology. When the supply of oxygen and solute exceeds the rate at which the crystal lattice can incorporate them, growth instabilities develop along the supersaturation gradient. This effect is most pronounced at particle corners, where localized solute fluxes promote dendritic extension and needle-like growth [38–40]. In situ HT-CSLM observations in the present study corroborate this behavior: elongated, branched inclusions formed preferentially during high-oxygen holding, consistent with unstable growth driven by supersaturation.

4.3 | Application of the Model

A revised version of the Paunov simplified model, as adopted from [16], was applied to compare theoretical capillary forces with experimental measurements. This comparison aimed to verify that the observed inclusion interactions are consistent with capillary attraction and to assess how well the model captures the underlying interaction behavior.

For the calculations, the density of Al–silicate inclusions was taken as 2815 kg/m^3, the density of liquid steel as 7000 kg/m^3, and the contact angle between them as 136°, based on [11]. Circularity (CF_k, Equation (1)) quantifies inclusion shape, while the kinematic analysis assumes spherical particles with a radius correction. For the two Al–silicate inclusions analyzed in Figure 5a–d ($CF_1 = 0.7$, $CF_2 = 0.9$), Newton's second law (Equations (2)–(5)) was applied using an effective radius to account for shape deviation. Previous studies [25, 28] showed that using the equivalent radius, R_k, for inclusions with low circularity can introduce significant errors in capillary force predictions. To address this, the effective radius, $R_{k,\mathrm{eff}}$, was introduced, derived from the perimeter P_k and circularity CF_k as:

$$R_{k,\mathrm{eff}} = \frac{P_k}{2\pi} = \frac{R_k}{\sqrt{CF_k}} \tag{13}$$

Figure 10 compares the experimental and theoretical attractive forces between Al–silicate inclusion pairs. The x-axis represents interparticle distance, and the y-axis shows the capillary force on a logarithmic scale. Triangles denote experimental data, while dashed lines represent model predictions using either the effective radius (red) or the equivalent radius (gray). Predictions based on the effective radius align closely with the experimental data, whereas those using the equivalent radius deviate.

These findings are consistent with Mu et al. [32], who reported that the effective radius provides better agreement for small inclusions (5–30 μm, circularity > 0.2), while the equivalent

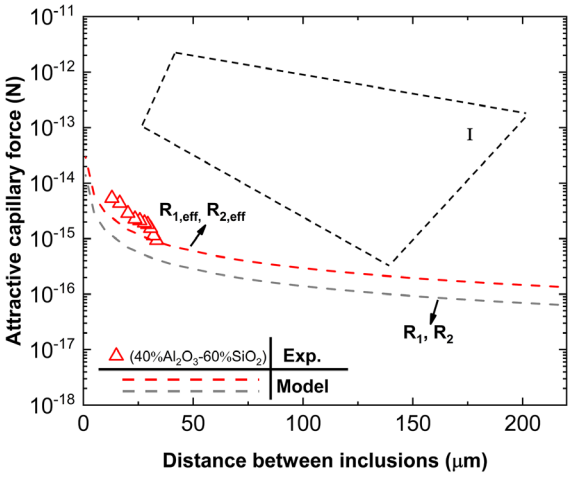

FIGURE 10 | Comparison of experimental and theoretical attractive forces between Al–silicate inclusion pairs. Triangles denote experimental data, while dashed lines represent model predictions using either the effective radius (red) or the equivalent radius (gray). For reference, the dashed polygon (I) shows calculations by Mu et al. [32] for an Al_2O_3 inclusion pair.

radius is more suitable for large, irregular inclusions (>40 μm, circularity < 0.2). In the current study, the Al–silicate inclusions analyzed fall within the small-to-medium size range (5–30 μm), and the model results using the effective radius closely match the measured data. Using the equivalent radius instead would underestimate the attractive force by a factor $1/\sqrt{CF_k}$, corresponding to ~20% and ~5% for CF_1 and CF_2, respectively, confirming the validity of the spherical assumption with circularity correction. This strong correlation confirms the suitability of the capillary force-based model for predicting inclusion interaction and agglomeration, though further validation across a broader range of sizes and morphologies is still needed.

Building on this validation, a comparative evaluation was carried out between the attractive forces observed in Al-killed steel containing Al_2O_3 inclusions [16] and those in Si-killed steel with Al–silicate inclusions from the present study. As shown in Figure 10, alumina inclusions (black dashed line) exhibit significantly stronger attractive forces, ranging from 10^{-15} to 10^{-11} N over a size range of 10–48 μm. In contrast, Al–silicate inclusions show notably weaker forces and a shorter interaction range, with a maximum effective acting length of 34 μm—approximately one-sixth that of Al_2O_3 pairs.

This pronounced difference highlights the reduced tendency of Al–silicate inclusions to agglomerate at the steel/gas interface as compared to alumina. The effect can be attributed to differences in composition and phase state. In the present study, higher silicon content promotes the formation of semiliquid/solid Al–silicate inclusions, whereas Al-killed steel primarily contains solid Al_2O_3 inclusions. The semiliquid/solid state alters interfacial characteristics by lowering interfacial energy and modifying the contact angle, thereby reducing the driving force for agglomeration. Furthermore, the density difference between solid and semiliquid/solid inclusions weakens interfacial interactions. Collectively, these factors contribute to the diminished agglomeration tendency observed for Al–silicate inclusions.

4.4 | Influence of Factors on the Interaction of Inclusion Particles

4.4.1 | Effect of Inclusion Size

To examine the influence of inclusion size on attractive capillary force, Mu's revised model [16] was applied. The values for the contact angle and interfacial tension between the inclusion and the liquid steel, as well as the density of the liquid steel, were consistent with those used in the experimental measurements. The radius of one of the inclusions, say, (R_1) was fixed at 17 μm, representing the radius of inclusion 1 in the experiments. Meanwhile, the radius of the other inclusion (R_2) varied between 1 and 100 (μm). The calculated results are presented in Figure 11.

Figure 11 illustrates that the attractive capillary force increases as the distance between inclusions decreases, regardless of the radius of the other inclusion (R_2). As the distance reduces from 80 to 10 μm, the attractive force increases by approximately one order of magnitude within each size group. According to the model described in Section 2.4, the attractive force is inversely proportional to the distance between inclusions. A decrease in distance results in a greater difference in liquid surface height (Δh) between the agglomerated inclusions and the surrounding liquid. Additionally, the attractive force increases by several orders of magnitude as R_2 increases from 1 to 100 μm. For instance, when R_2 is 1 μm, the attractive capillary force ranges between 8×10^{-20} and 6×10^{-19} N, and it rises to 6×10^{-13} N when R_2 reaches 100 μm. This indicates a stronger attraction between larger inclusions.

The size-dependent behavior described above plays a key role in evaluating the agglomeration potential of Al–silicate inclusions. At a practical separation distance of 34 μm, used here as a reference for comparing with alumina inclusions, the attractive capillary force becomes notably strong when the inclusion size reaches around 70 μm, as marked by the cross in Figure 11. At this point, the force reaches values that approach the same range (10^{-13} N) as Al_2O_3 inclusions in Al-killed steel, shown in Figure 10. This suggests that Al–silicate inclusions of 70 μm or larger may begin to exhibit similar agglomeration behavior

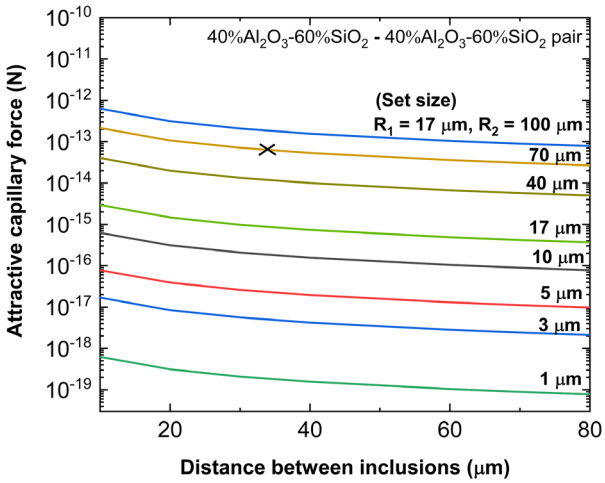

FIGURE 11 | Influence of inclusion size on the attractive capillary force of 40%Al_2O_3–60%SiO_2 Al–silicate inclusion pair, as predicted by the Paunov's model. The radius of one inclusion (R_1) was fixed at 17 μm, while the other (R_2) varied from 1 to 100 μm.

under comparable conditions. However, since this conclusion is based on modeled interactions, further validation through experiments or industrial-scale observations is necessary to determine whether such forces are sufficient to trigger agglomeration in real systems.

4.4.2 | Effect of Contact Angle

The revised model was used to calculate the attractive capillary force for inclusions with varying contact angles. Figure 12 compares the values for attractive capillary force with respect to the distance between inclusions. There is a good agreement between the prediction of the model and the experimental data obtained in this study using a contact angle of 136°. The calculation considered inclusions with the same radius and density as those used in the experiments, with relevant parameters already provided in Section 4.3.

The results show that higher contact angles (e.g., 120° and 136°) result in stronger capillary forces, while lower angles (e.g., 75°) yield weaker interactions. As inclusions transition from solid to semisolid, semiliquid, and eventually liquid phases, their contact angle decreases due to increased wettability in liquid steel. This results in weaker attractive forces between inclusions.

The contact angle thus plays a crucial role in inclusion agglomeration: higher contact angles promote stronger attraction, while lower angles favor dispersion. This underscores the importance of both the inclusion phase state and interfacial properties in governing agglomeration behavior.

4.5 | Nature of Attractive Force

Various attractive forces can influence interactions between nonmetallic inclusions. Zheng et al. [41] identified three primary mechanisms: van der Waals, gas cavity, and capillary forces. Van der Waals and gas cavity forces are only effective at extremely short distances (less than 1 μm), with magnitudes ranging from 10^{-11} to 10^{-10} N and 10^{-4} to 10^{-3} N, respectively. In contrast, capillary forces can act over longer distances—up to 100 μm [13], though they typically exhibit lower magnitudes (10^{-12} to 10^{-19} N).

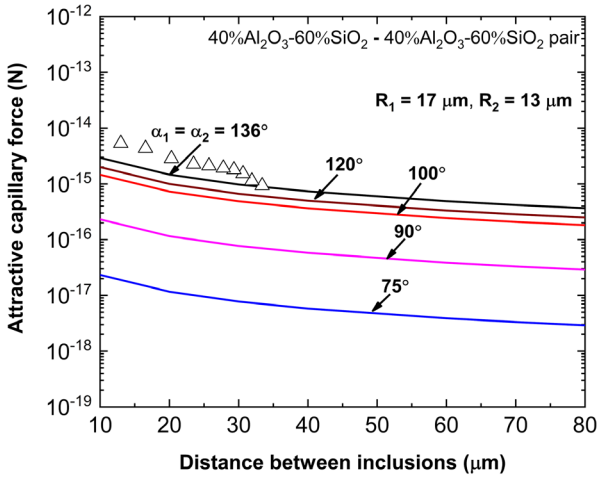

FIGURE 12 | Influence of contact angle between 75° and 136° on the attractive capillary force of 40%Al_2O_3–60%SiO_2 Al–silicate inclusion pair (R_1= 17 μm, R_2 = 13 μm), as predicted by the Paunov's model.

The experimentally derived forces in this study, which fall within the range of 10^{-16} to 10^{-15} N, are consistent with values expected for capillary forces, reinforcing their role as the dominant agglomeration mechanism at the steel/gas interface.

5 | Conclusions

This study examined the agglomeration behavior of semisolid Al–silicate inclusions in Si-killed steel. A synthetic steel sample containing 250 ppm oxygen was produced in a vertical tube furnace, characterized by SEM-EDS to identify inclusion types, and then examined by in situ HT-CLSM and by modeling to evaluate their interaction and agglomeration tendencies. The main conclusions are:

1. Inclusions transformed from spherical to irregular, needle-like morphologies through agglomeration of smaller particles and preferential growth of alumina under high oxygen conditions and prolonged holding. SEM-EDS confirmed their alumina-rich composition, consistent with thermodynamic predictions at 1873 K showing strong supersaturation of Al_2O_3.
2. Time-resolved tracking showed increasing velocity and acceleration as inclusions approached, confirming that their motion was driven by attractive capillary forces rather than bulk liquid flow.
3. Capillary forces between Al–silicate inclusions ranged from 10^{-16} to 10^{-15} N with a maximum acting length of ~34 μm, several orders of magnitude weaker and shorter-ranged than those reported for alumina inclusions. This reduced force indicates lower attraction at the steel/gas interface and explains their lower tendency to agglomerate at the steel/gas interface.
4. The simplified Paunov model, modified with an effective radius, reproduced the experimental force–distance relationships for Al–silicate inclusions. However, further validation is needed for larger and more irregular inclusion morphologies.

Overall, these findings demonstrate key differences between Al–silicate and alumina inclusion behavior, with direct implications for nozzle clogging and steel cleanliness. The reduced agglomeration tendency of Al–silicates highlights the importance of steel deoxidation practice and inclusion chemistry in determining interfacial interactions.

Author Contributions

Suwam Kumar: conceptualization (lead), formal analysis (lead), investigation (lead), methodology (lead), writing – original draft (lead). **Muhammad Nabeel:** formal analysis (supporting), methodology (supporting), writing – review and editing (supporting). **Angshuman Podder:** formal analysis (supporting), writing – review and editing (supporting). **Andre B. Phillion:** funding acquisition (lead), investigation (supporting), project administration (lead), supervision (equal), validation (supporting), writing – review and editing (supporting). **Neslihan Dogan:** conceptualization (supporting), investigation (supporting), supervision (equal), validation (supporting), writing – review and editing (supporting).

Acknowledgments

The authors gratefully recognize financial support from the Natural Sciences and Engineering Research Council of Canada (NSERC) and the McMaster Steel Research Centre (SRC). Support for materials characterization was provided by the Canadian Centre for Electron Microscopy (CCEM) at McMaster University.

Funding

This study was supported by Natural Sciences and Engineering Research Council of Canada.

Conflicts of Interest

The authors declare no conflicts of interest.

Data Availability Statement

The data that support the findings of this study are available from the corresponding author upon reasonable request.

References

1. A. Ghosh and A. Chatterjee, *Iron Making and Steelmaking: Theory and Practice* (PHI Learning Pvt. Ltd., 2008).

2. E. Pretorius, H. Oltmann, and B. Schart, *An Overview of Steel Cleanliness from an Industry Perspective* (AISTech Proceedings, 2013). 6–9.

3. H. Atkinson and G. Shi, "Characterization of Inclusions in Clean Steels: A Review including the Statistics of Extremes Methods," *Progress in Materials Science* 48, no. 5 (2003): 457–520.

4. R. B. Tuttle, J. D. Smith, and K. D. Peaslee, "Interaction of Alumina Inclusions in Steel with Calcium-Containing Materials," *Metallurgical and Materials Transactions B* 36 (2005): 885–892.

5. P. Misra, V. Chevrier, S. Sridhar, and A. Cramb, "In Situ Observations of Inclusions at the (mn, Si)-Killed Steel/Cao-al (2)o(3) Interface," *Metallurgical and Materials Transactions* 31, no. 5 (2000): 1135.

6. R. J. Fruehan, *The Making, Shaping and Treating of Steel.[2]. Steelmaking and Refining Volume* (AISE Steel Foundation, 1998).

7. G. Bernard, P. Riboud, and G. Urbain, "Étude De LA Plasticité d'inclusions d'oxydes," *Revue De Métallurgie* 78, no. 5 (1981): 421–434.

8. https://worldsteel.org/wp-content/uploads/worldsteel-book-final-2022-1.pdf, (2022).

9. A. Ghosh, *Secondary Steelmaking: Principles and Applications* (CRC Press, 2000).

10. S. Papadopoli Tone, "Non-metallic inclusion changes in si-mn killed steels," Ph.D. thesis (Carnegie Mellon University, 2018).

11. H. Yin, H. Shibata, T. Emi, and M. Suzuki, "In-Situ" Observation of Collision, Agglomeration and Cluster Formation of Alumina Inclusion Particles on Steel Melts," *ISIJ International* 37, no. 10 (1997): 936–945.

12. H. Yin, H. Shibata, T. Emi, and M. Suzuki, "Characteristics of Agglomeration of Various Inclusion Particles on Molten Steel Surface," *ISIJ International* 37, no. 10 (1997): 946–955.

13. Y. Tanaka, F. Pahlevani, and V. Sahajwalla, "Agglomeration Behavior of Non-Metallic Particles on the Surface of Ca-Treated High-Carbon Liquid Steel: An In Situ Investigation," *Metals* 8, no. 3 (2018): 176.

14. Y. Tanaka, F. Pahlevani, S.-Y. Kitamura, K. Privat, and V. Sahajwalla, "Behaviour of Sulphide and Non-Alumina-Based Oxide Inclusions in Ca-Treated High-Carbon Steel," *Metallurgical and Materials Transactions B* 51 (2020): 1384–1394.

15. S. Vantilt, B. Coletti, B. Blanpain, J. Fransaer, P. Wollants, and S. Sridhar, "Observation of Inclusions in Manganese-Silicon Killed Steels at Steel-Gas and Steel-Slag Interfaces," *ISIJ International* 44, no. 1 (2004): 1–10.

16. W. Mu, N. Dogan, and K. S. Coley, "Agglomeration of Non-Metallic Inclusions at Steel/Ar Interface: In-Situ Observation Experiments and Model Validation," *Metallurgical and Materials Transactions B* 48 (2017): 2379–2388.

17. A. Podder, "Modelling transient inclusion behaviour during refining of si-mn killed steel," Ph.D. thesis, Dissertation (McMaster University, 2023).

18. V. Paunov, P. Kralchevsky, N. Denkov, and K. Nagayama, "Lateral Capillary Forces between Floating Submillimeter Particles," *Journal of Colloid and Interface Science* 157, no. 1 (1993): 100–112.

19. H. Chikama, H. Shibata, T. Emi, and M. Suzuki, ""In-Situ" Real Time Observation of Planar to Cellular and Cellular to Dendritic Transition of Crystals Growing in Fe–c Alloy Melts, Materials Transactions," *JIM* 37, no. 4 (1996): 620–626.

20. W. Mu, P. G. Jönsson, and K. Nakajima, "Prediction of Intragranular Ferrite Nucleation from Tio, Tin, and Vn Inclusions," *Journal of Materials Science* 51 (2016): 2168–2180.

21. B. Monaghan and L. Chen, "Dissolution Behavior of Alumina Micro-Particles in Cao-Sio2-Al2o3 Liquid Oxide," *Journal of Non-Crystalline Solids* 347, no. 1 (2004): 254–261.

22. W. Mu, H. Shibata, P. Hedström, P. Jönsson, and K. Nakajima, "Dissolution Behavior of Alumina Micro-Particles in Cao-Sio2-Al2o3 Liquid Oxide," *Metallurgical Materials Transaction B* 47B (2016): 2133–2147.

23. S. Griesser and R. Dippenaar, "Enhanced Concentric Solidification Technique for High-Temperature Laser-Scanning Confocal Microscopy," *ISIJ International* 54, no. 3 (2014): 533–535.

24. C. A. Schneider, W. S. Rasband, and K. W. Eliceiri, "Nih Image to Imagej: 25 Years of Image Analysis," *Nature Methods* 9, no. 7 (2012): 671–675.

25. K. Nakajima and S. Mizoguchi, "Capillary Interaction between Inclusion Particles on the 16cr Stainless Steel Melt Surface," *Metallurgical and Materials Transactions B* 32 (2001): 629–641.

26. S. Kimura, K. Nakajima, and S. Mizoguchi, "Behavior of Alumina-Magnesia Complex Inclusions and Magnesia Inclusions on the Surface of Molten Low-Carbon Steels," *Metallurgical and Materials Transactions* 32, no. 1 (2001): 79.

27. J. Appelberg, K. Nakajima, H. Shibata, A. Tilliander, and P. Jönsson, "In Situ Studies of Misch-Metal Particle Behavior on a Molten Stainless Steel Surface," *Materials Science and Engineering: A* 495, no. 1-2 (2008): 330–334.

28. J. Wikström, K. Nakajima, H. Shibata, A. Tilliander, and P. Jönsson, "In Situ Studies of Agglomeration between Al2o3–cao Inclusions at Metal/Gas, Metal/Slag Interfaces and in Slag," *Ironmaking & Steelmaking* 35, no. 8 (2008): 589–599.

29. P. Kralchevsky, V. Paunov, N. Denkov, I. Ivanov, and K. Nagayama, "Energetical and Force Approaches to the Capillary Interactions between Particles Attached to a Liquid-Fluid Interface," *Journal of Colloid and Interface Science* 155, no. 2 (1993): 420–437.

30. K. Ogino, A. Adachi, and K. Nogi, "The Wettability of Solid Oxides by Liquid Iron," *Tetsu-to-Hagané* 59 (1237): 1973.

31. W. Chen, D. de Kee Fong, and P. N. Kaloni, *Advanced Mathematics for Engineering and Science* (World Scientific, 2003).

32. W. Mu, N. Dogan, and K. S. Coley, "Agglomeration of Non-Metallic Inclusions at the Steel/Ar Interface: Model Application," *Metallurgical and Materials Transactions B* 48 (2017): 2092–2103.

33. W. Mu and C. Xuan, "Agglomeration Mechanism of Complex Ti-al Oxides in Liquid Ferrous Alloys considering High-Temperature Interfacial Phenomenon," *Metallurgical and Materials Transactions B* 50 (2019): 2694–2705.

34. T. Braun, J. Elliott, and M. Flemings, "The Clustering of Alumina Inclusions," *Metallurgical Transactions B* 10 (1979): 171–184.

35. J. F. Elliott, M. Gleiser, and V. Ramakrishna, *Thermochemistry for Steelmaking*, Vol. II (Addison Wesley, 1963).

36. G. K. Sigworth and J. F. Elliott, "The Thermodynamics of Liquid Dilute Iron Alloys," *Metal Science* 8, no. 1 (1974): 298–310.

37. H. Gaye, C. Gatellier, M. Nadif, P. V. Rivoud, J. Saleil, and M. Faral, *Revue de Métallurgie - Cahiers d'Informations Techniques* 84 (1987): 759.

38. M. C. Flemings, "Solidification Processing," *Metallurgical and Materials Transactions B* 5 (1974): 2121–2134.

39. D. M. Stefanescu, *Science and Engineering of Casting Solidification* (Springer, 2015).

40. J. S. Langer, "Instabilities and Pattern Formation in Crystal Growth," *Reviews of Modern Physics* 52, no. 1 (1980): 1.

41. L. Zheng, A. Malfliet, P. Wollants, B. Blanpain, and M. Guo, "Effect of Alumina Morphology on the Clustering of Alumina Inclusions in Molten Iron," *ISIJ International* 56, no. 6 (2016): 926–935.